



Influence of Configuration on Materials Selection for Actively Cooled Combustors

N. Vermaak*

University of California, Santa Barbara, Santa Barbara, California 93106-5050

L. Valdevit†

University of California, Irvine, Irvine, California 92697-3975

and

A. G. Evans‡

University of California, Santa Barbara, Santa Barbara, California 93106-5050

DOI: 10.2514/1.45417

The influence of combustor size and shape on material feasibility is explored using (structural and fuel) weight, as well as fuel economy as metrics. A materials selection methodology developed for actively cooled rectangular panels has been embellished to include cylindrical/annular configurations. The procedure incorporates an analytical model for temperature and stress distributions subject to thermomechanical loads representative of hypersonic flight conditions. The model has been numerically verified using finite element simulations. By combining the model with optimization routines, materials robustness maps have been produced, depicting the range of thermal loads and fuel flow rates that satisfy all design constraints. A wide selection of high-temperature materials has been investigated. Comparisons of cylindrical and rectangular combustors are made for the leading candidates. It is established that the cylindrical designs allow both lighter optimal structures as well as greater robustness and fuel economy.

Nomenclature

A	=	area, m ²
B	=	width of the actively cooled panel, m
C	=	cylindrical/annular model
D	=	diameter, m
E	=	Young's modulus, Pa
f	=	fuel/air mass ratio
H	=	thickness, m
h	=	heat transfer coefficient, W/m ² · K
k	=	thermal conductivity, W/m · K
L	=	height of the cooling channel, m
l	=	length scale associated with upstream onset of boundary layer, m
M	=	analytical model
M	=	mass, kg
N	=	numerical
p	=	pressure, Pa
q	=	dynamic pressure, Pa
R	=	combustor radius, m
R	=	rectangular model
r	=	cylindrical spatial coordinate
r	=	radius, m
T	=	temperature, K
t	=	thickness, m
u	=	displacement, m
V	=	air velocity, m/s
\dot{V}	=	volumetric flow rate of the coolant, m ³ /s
W	=	width of the cooling channel, m
x, y, z	=	spatial coordinates
Z	=	altitude, km

Z	=	length of the actively cooled panel, m
α	=	thermal expansion coefficient, ppm/K
Δ	=	difference
ε	=	strain
θ	=	cylindrical spatial coordinate
Λ	=	extra mass ratio
ν	=	Poisson's ratio
π	=	pi
ρ	=	mass density, kg/m ³
σ	=	normal stress, Pa
σ_{ult}	=	critical strength of a ceramic matrix composite material, MPa
σ_{yield}	=	yield strength of a metallic material, MPa
ζ	=	spatial coordinate at midpoint of internal face, oriented radially
ϕ	=	equivalence ratio (actual fuel/air ratio divided by stoichiometric fuel/air ratio)
χ	=	combustion heat transfer ratio (actual/expected steady-state value)

Subscripts

air	=	relative to captured air in the combustor
aw	=	adiabatic wall conditions
$c, cool$	=	relative to the cooling channels
comb	=	within the combustion chamber
cyl	=	pertaining to the cylindrical model
EA	=	assuming combustors of equal area
$f, face$	=	relative to the face sheet
$f, fuel$	=	relative to the fuel (coolant)
fillet	=	describing fillet radius
G	=	relative to the hot gases in the combustion chamber
i	=	relative to the internal cylindrical face sheet
m	=	at the middle of the cylindrical unit cell
min	=	minimum
o	=	relative to the external cylindrical face sheet
panel	=	relative to the whole cross section of the panel
r, θ, z	=	along the respective cylindrical directions
rect	=	pertaining to the rectangular model
s	=	relative to the solid
ss	=	steady state

Received 12 May 2009; revision received 2 November 2009; accepted for publication 2 November 2009. Copyright © 2009 by the American Institute of Aeronautics and Astronautics, Inc. All rights reserved. Copies of this paper may be made for personal or internal use, on condition that the copier pay the \$10.00 per-copy fee to the Copyright Clearance Center, Inc., 222 Rosewood Drive, Danvers, MA 01923; include the code 0748-4658/10 and \$10.00 in correspondence with the CCC.

*Ph.D. Candidate, Materials Department. Student Member AIAA.

†Assistant Professor, Mechanical and Aerospace Engineering/Chemical Engineering and Materials Science Departments. Member AIAA.

‡Professor, Materials/Mechanical Engineering Departments.

shape	= referring to rectangular or cylindrical/annular configurations
st	= stoichiometric
w	= relative to the unit-cell core web
x, y, z	= along the respective rectilinear coordinates
0	= inlet conditions
1–9	= relative to the respective point in the unit cell
3	= pertaining to the combustor location in the vehicle

Superscripts

bend	= bending stresses
c	= relative to the core web
i	= relative to the internal cylindrical face sheet
i	= relative to one of the nine unit-cell locations monitored
o	= relative to the external cylindrical face sheet
ref	= reference mass
w	= relative to the unit-cell core web
*	= maximum use

I. Introduction

SCRAMJET engine design has evolved without a common configuration [1,2]. Flowpath systems have ranged from three to two dimensional, including inward turning and planar configurations [1,2]. Among these options, the cylindrical configuration has the attribute that its aerodynamic shape control, viscous losses, and pressure resistance are superior to rectangular designs [3]. It remains to establish relationships that allow preferred materials to be selected on the basis of combustor shape and size. The present article provides these relationships by developing solutions for cylindrical combustors and comparing with previous derivations for rectangular designs [4,5]. Although cylindrical configurations have been largely restricted to small vehicles, recent assessments suggest broader potential for larger scales [2,3].

The combustion chamber has internal surfaces devoid of radiative cooling. Consequently, active cooling is needed to contend with high combustion heat fluxes and/or aerodynamic heating, exemplified by the combustor of a Mach 7 airbreathing hypersonic vehicle cooled by hydrocarbon fuel (Fig. 1). Representative rectangular and cylindrical/annular designs are depicted in Fig. 1, with an illustration of the thermomechanical loading. In such a structure, before injection, the fuel passes through internal channels in the combustor walls. In the present article, the effect of combustor shape and size on

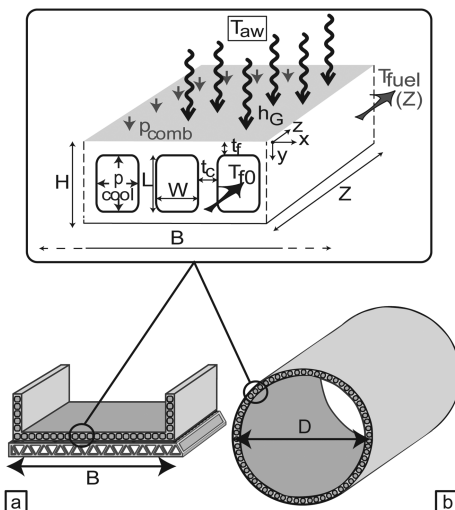


Fig. 1 Schematic of an actively cooled hypersonic combustor panel with thermostructural loads indicated: a) rectangular configuration, and b) generalized annular/cylindrical configuration. The mechanical loads comprise the combustion pressure, p_{comb} , and the coolant pressure, p_{cool} . The thermal load is convective and described by the adiabatic wall temperature, T_{aw} , and the combustion heat transfer coefficient, h_G .

Table 1 Vehicle types analyzed with HAP [6]

Parameter ^a	Three-shock system [4]	One-shock system
Mach	7	7
q_0	47.8 kPa	47.8 kPa
Z_0	30 km	30 km
f_{st} (JP-7)	0.0675 kg _{fuel} /kg _{air}	0.0675 kg _{fuel} /kg _{air}
T_3/T_0	5.6	5.6
A_3/A_0	0.059	0.2668
p_{comb}	0.16 MPa	0.036 MPa
T_{aw}	3050 K	3000 K
l	6 m	0.345 m
h_G	445 W/m ² · K	250 W/m ² · K

^aNot all parameters listed are independent.

the ability of these panels to withstand the thermomechanical loading is explored using (structural and fuel) weight, as well as fuel economy, as metrics. The approach replicates a materials selection and optimization methodology previously developed for rectangular configurations [4]. Robustness maps that depict the range of thermal loads and fuel flow rates satisfying all design constraints are produced for Mach 7 hydrocarbon-fueled flight. Such maps establish the advantages and disadvantages of cylindrical and rectangular designs from a materials perspective.

To effectively compare different combustor shapes, aspects of vehicle design and integration must be considered. A preliminary comparison will be conducted on a three-shock system [6] previously used for the rectangular panel. However, because annular vehicles are better approximated as smaller one-shock systems [1,6], the comparison is extended to both options. The software known as hypersonic airbreathing propulsion (HAP) [6] is used to define the thermophysical properties of the airflow throughout the vehicle, for both (three- and one-shock) systems. Some of the assumptions and conditions characterizing the vehicles are listed in Table 1. Note that, for the rectangular design, bending due to the combustion pressure has adverse consequences unless suppressed by attaching a stiff sandwich panel (Fig. 1), which adds weight. The associated mass is regarded here as a second-order complexity and not taken into account. This is not an issue for the cylindrical configuration, which does not experience bending. Note that both configurations allow thermal expansion along all three dimensions, whereas thermal bending is restricted (generalized plane strain).

The article is organized as follows. A synopsis of the physical model is presented and the model verified. The rectangular and cylindrical models are compared in terms of 1) resistance to thermal and mechanical loads, 2) relative magnitude of critical stresses, and 3) the effect of combustor size. A preliminary set of shape comparisons is conducted using both the three- and one-shock systems.

II. Cylindrical Model

The model uses a thermal resistance network scheme to analytically predict temperatures throughout the panel. Simultaneously, the model predicts the thermoelastic stresses using a combination of beam/plate theory. A viable structure must resist the following failure modes, yielding or rupture due to 1) thermal stresses, 2) pressure or inertial stresses, 3) and combined thermomechanical stresses, as well as 4) softening of the material, 5) coking of the coolant, and 6) an excessive pressure drop in the cooling ducts. The challenge is to assure that none of the failure modes are active over the pertinent ranges of the coolant flow rate, \dot{V} , and of the heat transfer coefficient between the combustion gas and the solid surface, h_G (Fig. 1). For convenience, these terms are expressed nondimensionally. The normalized flow rate is unity, $\phi = \dot{V}/\dot{V}_{st} = 1$, when all of the fuel needed for stoichiometric combustion is used for combustor cooling. Larger values imply that excess fuel is needed just for cooling and smaller values that some of the fuel is used for cooling other parts of the vehicle or the combustor may run lean. Note that the fuel flow parameter can also be an indirect

measure of 1) the fuel weight carried by the vehicle or 2) the fuel economy. The normalized heat transfer coefficient is unity, $\chi = h_G/h_{G,ss} = 1$, when the combustor is operating at steady state, without hot spots from shock waves. Larger values allow for the possibility of hot spots and project performance to higher-Mach-number operations. Although this simplified characterization of heat transfer between the combustion gas and the walls is unable to capture shape-dependent boundary-layer effects that may further augment heat transfer, it nevertheless provides a baseline from which to determine the influence of the configuration on minimum weight designs. An optimization protocol that addresses this multivariable, nonlinear problem [4] will be implemented.

A. Axial Stresses

Combined panel-level thermal gradient and pressures: The temperature drop across the panel, measured from the internal to the external face, is (Fig. 2)

$$\Delta T_{\text{panel}} = \frac{(T_1 + T_2 + T_5 + T_6)}{4} - \frac{(T_3 + T_4 + T_7 + T_8)}{4} \quad (1)$$

Determination of the 12 nonnegligible stresses and strains requires solutions for the following independent equations, subject to generalized plane strain, $\epsilon_z^i = \epsilon_z^o = \epsilon_z^w$.

Constitutive equations:

$$\begin{aligned} \epsilon_r^w &= (1/E)(\sigma_r^w - \nu\sigma_z^w), & \epsilon_z^w &= (1/E)(\sigma_z^w - \nu\sigma_r^w) \\ \epsilon_\theta^o &= (1/E)(\sigma_\theta^o - \nu\sigma_z^o), & \epsilon_z^o &= (1/E)(\sigma_z^o - \nu\sigma_\theta^o) \\ \epsilon_\theta^i &= (1/E)(\sigma_\theta^i - \nu\sigma_z^i) + \alpha\Delta T_{\text{panel}} \\ \epsilon_z^i &= (1/E)(\sigma_z^i - \nu\sigma_\theta^i) + \alpha\Delta T_{\text{panel}} \end{aligned} \quad (2)$$

Compatibility:

$$\epsilon_r^w = \frac{\Delta H}{H} = \frac{(\Delta D_i/2) - (\Delta D_o/2)}{(D_i - D_o)/2} = \frac{D_i\epsilon_\theta^i - D_o\epsilon_\theta^o}{(D_i - D_o)} \quad (3)$$

Equilibrium:

$$\begin{aligned} 2\sigma_\theta^o t_f + 2\sigma_\theta^i t_f - D_i p_{\text{comb}} &= 0 \quad (\text{along } \theta) \\ \sigma_\theta^i &= \underbrace{\left(\frac{\sigma_r^w t_w}{(W_m + t_w)} \right)}_{\text{Effective pushback web pressure}} \frac{D_i}{2t_f} + \left(p_{\text{comb}} - p_{\text{cool}} \frac{W_m}{(W_m + t_w)} \right) \frac{D_i}{2t_f} \quad (\text{along } r) \\ \sigma_z^o t_f \pi D_o + \sigma_z^i t_f \pi D_i + \sigma_z^w t_w L \frac{\pi D_i}{(W_m + t_w)} &= 0 \quad (\text{along } z) \end{aligned} \quad (4)$$

Here, θ , r , and z represent the hoop, radial, and longitudinal directions in cylindrical coordinates; i , o , and w denote the inner and outer face and the core web; E , ν , and α are Young's modulus, Poisson's ratio, and the coefficient of thermal expansion of the material; and the geometric parameters are defined in Fig. 1. The resulting stress expressions are too cumbersome to explicitly list, but are directly incorporated in the optimization scheme [4].

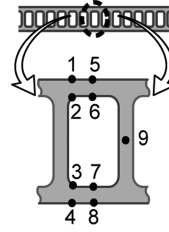
Thermal gradient across internal face (ΔT_{face}): The temperature drop across the internal face (Fig. 2, in the radial direction) is essentially linear and modeled as $\Delta T_{\text{face}} = T_5 - T_6$, with T_5 and T_6 chosen because the highest gradients typically exist at this location [4]. The thermal stresses are

$$\sigma_{rr} = 0, \quad \sigma_{\theta\theta} = \sigma_{zz} = \frac{E\alpha\Delta T_{\text{face}}}{2(1-\nu)} \left(\frac{2\zeta}{t_f} \right) \quad (5)$$

where ζ is the coordinate centered at the midpoint of the internal face, in the radial direction. *The internal face is treated as a discrete cylinder; its thermal stresses are superimposed on those found from Eqs. (2–4).*

B. Bending Stresses

Bending due to the combustion pressure is neglected because of the order of magnitude difference between p_{cool} and p_{comb} . There is



a RECTANGULAR MODEL
Sign of Contributing Stresses (x,z)

Points in Panel	ΔT_{panel}	ΔT_{face}	Pcool bend
1	-	-	-
2	-	+	+
3	+	n/a	+
4	+	n/a	-
5	-	-	+
6	-	+	-
7	+	n/a	-
8	+	n/a	+
9	$n/a^{(x)}$ +(z)	n/a	n/a

b CYLINDRICAL MODEL
Sign of Contributing Stresses (θ, z)

Points in Panel	ΔT_{panel}	ΔT_{face}	Pcool bend	P comb	P cool
1	-	-	-	+	-
2	-	+	+	+	-
3	+	n/a	+	+	+
4	+	n/a	-	+	+
5	-	-	+	+	-
6	-	+	-	+	-
7	+	n/a	-	+	+
8	+	n/a	+	+	+
9	$n/a^{(\theta)}$ +(z)	n/a	n/a	n/a	n/a

Fig. 2 Unit cell susceptible to local yielding and nine points monitored; a catalogue of the component stress signs for points: a) rectangular model, and b) cylindrical model.

one remaining contribution: coolant pressure (p_{cool}). The distributed pressure load along the length of the face beams (Fig. 1) is estimated by ignoring the curvature (the radius of the cylinder substantially exceeds >40 times the depth of its cross section [7]). The solution from the rectangular panel model [4] is used with a slight modification to account for the different effective beam lengths between the internal and external faces. Consistent with beam analysis, the through-thickness stresses (radial) are neglected, yielding

$$\begin{aligned} \sigma_{\theta\theta} &= -\frac{p_{\text{cool}}}{2} \left(\frac{W}{t_f} \right)^2 \text{ at points 1, 4; } \quad \frac{p_{\text{cool}}}{2} \left(\frac{W}{t_f} \right)^2 \text{ at points 2, 3;} \\ \sigma_{\theta\theta} &= \frac{p_{\text{cool}}}{4} \left(\frac{W}{t_f} \right)^2 \text{ at points 5, 8; } \quad -\frac{p_{\text{cool}}}{4} \left(\frac{W}{t_f} \right)^2 \text{ at points 6, 7;} \quad (6) \\ \sigma_{zz} &= \nu\sigma_{\theta\theta} \text{ for all points} \end{aligned}$$

where W is the width at the middle of the internal face for points 1, 2, 5, and 6 and the external face for points 3, 4, 7, and 8.

III. Model Verification

The accuracy of the model has been verified with a select number of finite element simulations, using the commercial software ABAQUS®. The cross section at the outlet ($z = Z$) was used, incorporating properties for the Ni-based superalloy, INCONEL X-750 (Table 2), subject to lean fuel flow conditions ($\phi = 0.6$). Near-optimal geometries have been used, resulting in the following unit-cell dimensions: $H = 5.8$ mm, $W_m = 3.59$ mm, $L = 5$ mm, and $t_f = t_c = 0.4$ mm. The internal corners were rounded ($r_{\text{fillet}} = 0.1$ mm) to avoid excessive stress intensification. The mesh with geometric parameters and boundary conditions is presented in Fig. 3. Quadratic (coupled temperature-displacement) generalized plane strain elements with reduced integration (CPEG8RHT) were used. Convective boundary conditions were applied to the internal face ($h_G = 445$ W/m² · K, $T_{\text{aw}} = 3050$ K), as well as on the inside surfaces ($h_c = 1744$ W/m² · K, $T_f = 731$ K). The remainder of the cell perimeter was thermally insulated. A pressure $p_{\text{cool}} = 4$ MPa was applied on the inside walls. The pressure in the combustion chamber, $p_{\text{comb}} = 0.16$ MPa, was applied to the internal face. Periodic boundary conditions were imposed (one side was constrained against translation in the circumferential direction, whereas all nodes on the other side were required to displace equally in the circumferential direction). The initial (stress-free) temperature was $T_{f0} = 400$ K.

A comparison of the steady-state temperature distributions (Table 3) reveals that the maximum temperature in the structure is captured within less than 1%. Moreover, the temperature differences governing the thermal stresses (ΔT_{panel} , ΔT_{face}) deviate by <8%. Contour plots of the von Mises stresses (Fig. 4), at critical locations, monitor the stress state of the panel under 1) combined thermomechanical loading, 2) thermal-only, and 3) mechanical-only conditions. It is insufficient to examine only the combined stresses, because the thermal and mechanical stresses have opposite signs in some locations (Fig. 2). To the left of each contour plot is a comparison of the analytic and numerical results at the three points of highest stress. The agreement is within 5% at the most highly stressed location (point 1). A full account of the stresses at each point is given in Table 4. The largest disagreements occur at the corners (points 2 and 3), which exhibit stress intensification. The disagreement is disregarded for two reasons: 1) local plasticity will redistribute the stresses and ameliorate the concentration, and 2) the radius can be increased to reduce the stresses. Disagreements also exist under mechanical-only loading, but the percentage discrepancies are tempered by the low magnitudes of the stresses, and occur for cases in which the model is mostly conservative. Corresponding comparisons

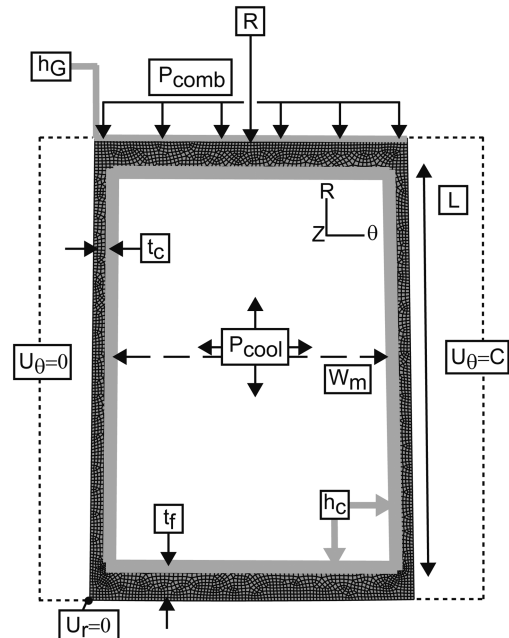


Fig. 3 Finite elements mesh used for calculations conducted using the properties of INCONEL X-750, indicating the geometry, loading, and boundary conditions.

performed for different materials and geometries (not presented) affirm that the analytical model captures temperature and stress distributions to the same level of accuracy.

IV. Preliminary Assessment of the Effects of Combustor Shape

This assessment is conducted for the three-shock design (Table 1). The comparison invokes the loading conditions derived for the rectangular combustor [4] and applies them to a cylindrical combustor of the same area. The unit-cell dimensions were listed earlier; note that the unit-cell width for the rectangular model was set equal to the centerline width of the cylindrical model. The shape affects two aspects of the physical models: 1) cooling capacity, and 2) stress analysis. It influences cooling capacity through the coolant velocity and heat transfer coefficient within the internal channels. These terms depend on the unit-cell dimensions (in this case, fixed), the actively cooled perimeter, and the volumetric coolant flow rate, \dot{V} :

Table 2 Candidate materials and their thermomechanical properties

Material	T^* , K	$\sigma_{\text{yield,ult}}(T^*)$, MPa	$d\sigma_{\text{yield}}/dT^{(i)}$, MPa/K	E , GPa	CTE, ppm/K	k_s , W/m · K	ρ_s , kg/m ³
Inconel X750	1100 ^a	527	-0.4	130	16.0	23	8276
C-103	1365	138	-0.1	85	7.0	35	8860
GrCOP-84	970	100	-0.2	90	19.0	285	8756
C-SiC	1810	200	—	100	2.0	15 (), 5(⊥)	2000
TBC (ZrO ₂)	—	—	—	—	—	1	3000

^aAggressive T^* values were chosen for the candidate materials.

Table 3 Comparison of model/numerical temperature distribution in unit-cell analysis

Locations in Panel	1	2	3	4	5	6	7	8	9
M	998	961	752	752	1092	1079	752	752	783
N	1036	1003	744	743	1082	1070	740	740	786
Absolute difference ($N - M$)	39	42	-8	-9	-9	-9	-12	-12	3
Percent difference ($(N - M)/N$)	4%	4%	-1%	-1%	-1%	-1%	-2%	-2%	0%

Table 4 Comparison of model/numerical von Mises stress distribution in unit-cell analysis

Locations in Panel	1	2	3	4	5	6	7	8	9
Net thermomechanical von Mises stress, MPa									
<i>M</i>	575	403	527	262	458	493	323	457	164
<i>N</i>	559	302	310	407	499	528	407	477	150
Absolute difference (<i>N</i> – <i>M</i>)	–16	–101	–217	145	41	35	84	20	–14
Percent difference (<i>N</i> – <i>M</i>)/ <i>N</i>	–3%	–33%	–70%	36%	8%	7%	21%	4%	–9%
Thermal-only von Mises stress, MPa									
<i>M</i>	498	462	366	366	498	462	366	366	179
<i>N</i>	483	301	245	477	546	493	455	393	161
Absolute difference (<i>N</i> – <i>M</i>)	–15	–161	–121	111	48	31	89	27	–18
Percent difference (<i>N</i> – <i>M</i>)/ <i>N</i>	–3%	–53%	–50%	23%	9%	6%	19%	7%	–11%
Mechanical-only von Mises stress, MPa									
<i>M</i>	109	168	178	119	99.1	41	45.6	104	34.7
<i>N</i>	89.8	164	169	78.3	99.9	50.9	54	108	37.7
Absolute difference (<i>N</i> – <i>M</i>)	–19	–4	–9	–41	1	10	9	4.0	3
Percent difference (<i>N</i> – <i>M</i>)/ <i>N</i>	–22%	–2%	–5%	–52%	1%	20%	16%	4%	8%

$$\dot{V} = \frac{f_{st}\phi\rho_0V_0A_0}{\rho_f} = 0.003281(A_0)\phi \text{ m}^3/\text{s} \quad (7)$$

where $f_{st} = \rho_f \dot{V}_{f, st} / \rho_{air} \dot{V}_{air, st}$ is the stoichiometric fuel/air ratio for JP-7 fuel (Table 1). The freestream conditions at Mach 7 and 30 km, denoted by the subscript 0, are reported elsewhere [4]. The flow rate varies with the size of the capture area (A_0), but not with the combustor shape. The actively cooled perimeter changes with shape: the cylindrical design always has less perimeter for the same area. For fixed unit-cell dimensions then, the cylindrical cooling velocity and heat transfer coefficient are greater. However, due to the nonlinear

nature of the optimization, it is not possible to determine a priori the trend in performance with shape.

The influence of shape on the stress analysis is more straightforward. A catalogue of the stress components for the two shapes is summarized in Fig. 2. Because of symmetry, only nine points are monitored. In the rectangular model, the stresses arise from three different loads: 1) ΔT_{panel} : axial thermal stresses from the panel-level thermal gradient, 2) ΔT_{face} : axial thermal stresses from the hot-face through-thickness temperature gradient, and 3) p_{cool}^{bend} : bending stresses from the coolant pressure. In the cylindrical model, the stresses arise from five different loads: 1) ΔT_{panel} : axial thermal stresses from the panel-level thermal gradient, 2) ΔT_{face} : axial thermal stresses from the hot-face through-thickness temperature gradient, 3) p_{cool}^{bend} : bending stresses from the coolant pressure, 4) p_{cool} : axial mechanical stresses from the coolant pressure, and 5) p_{comb} : axial mechanical stresses from the combustion pressure. In the rectangular model, point 1 is highlighted because all stress contributors are active and reinforce. For the cylindrical model, most of the stress contributors also reinforce at point 1 (in the z direction).

The combined effect of shape on cooling capacity and stress analysis for one of the locations most susceptible to failure, point 1, is presented on Fig. 5. For this case, the effects are confined to the influence of coolant velocity (a function of the actively cooled perimeter) by analyzing equivalent unit cells. Absolute values of each stress contribution normalized by the total absolute value stresses represent their relative roles in both models. Cursory examination of the charts reveals the expected similarity that the largest contribution to the stress is from ΔT_{panel} , followed by p_{cool}^{bend} , and then ΔT_{face} .

To highlight the key effects, emphasis has been placed on the largest contribution to stress, that from ΔT_{panel} , by using a representative thermal profile, wherein the internal face was set uniformly to 700 K (eliminating ΔT_{face}) and the rest of the structure was retained at 400 K (Fig. 6). The same unit-cell dimensions were used, with minimum allowable panel height, $H_{min} = 5.8$ mm [4,5]. Pressures were not active in this analysis, allowing examination of the effect of shape purely on the basis of relative magnitudes of critical stresses in the model. Differences in thermally induced von Mises stresses at the internal and external faces, as a function of the combustor radius, provide the requisite information. A reference radius, R_{EA} , was used to ensure equal area between the models, encompassing the range $1/20 \rightarrow 1000R_{EA}$. Notice that the difference between the two stress distributions decreases as the radius of the circular combustor increases. Namely, the stress distribution in the rectangular combustor is the limit of the stress distribution in the cylindrical combustor for $R \rightarrow \infty$. This is clearly shown in Fig. 6. Two regimes emerge (Fig. 6): regime I, in which the cylindrical model is highly sensitive to combustor radius; and regime II, in which the cylindrical model is insensitive to combustor radius and equivalent to the rectangular model. The reference design (equal cylindrical combustor area for the three-shock vehicle) lies

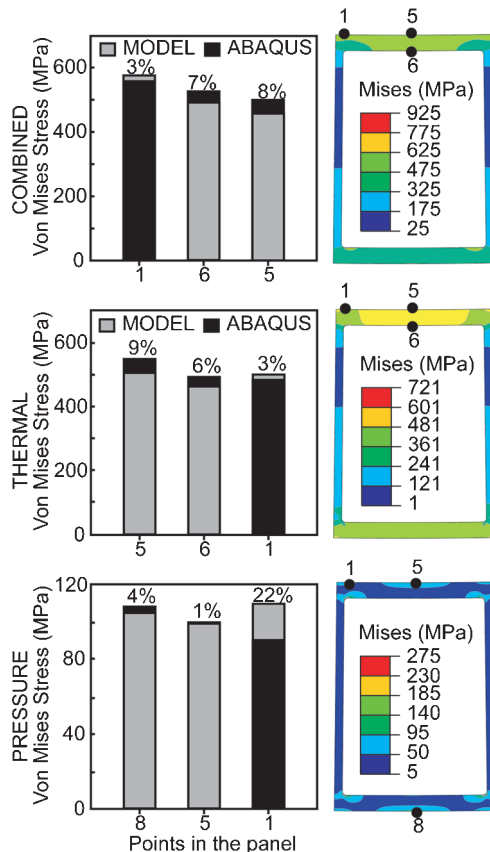


Fig. 4 Comparison of analytical and numerical von Mises stress distributions for the analysis of Fig. 3 (INCONEL X-750). The plots compare analytical and numerical predictions for thermal, mechanical, and thermomechanical stresses at the three points of highest stress.

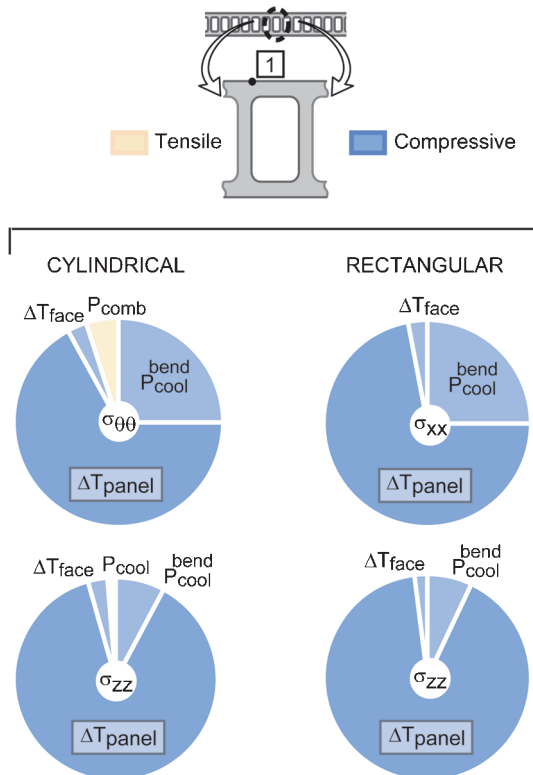


Fig. 5 Comparison of the relative contributions to stress for point 1. The conditions are the same as those for the finite element in Fig. 3. The pie charts show the absolute value of the stress contributions, normalized by the total absolute stress at the point, with tension (yellow) or compression (blue) indicated.

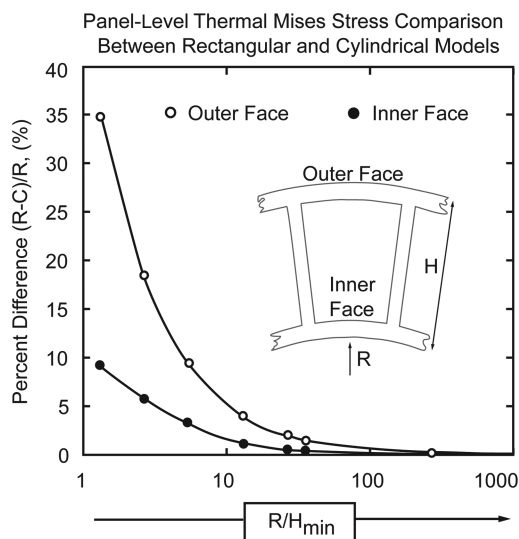


Fig. 6 Percentage difference between the rectangular (R) and cylindrical model (C) thermal stress predictions as a function of combustor radius.

within the transition between these regimes. Thus, the simpler rectangular model can be used to conservatively probe material performance for the larger hypersonic vehicles envisioned, whereas, for smaller missiles and some WaveRider®-type vehicles [8–10], assessments require implementation of the full cylindrical/annular model.

V. Influence of Combustor Shape on Minimum Weight

The cylindrical model has been incorporated into an optimization protocol [4] that seeks the minimum weight panel that resists all

failure modes, ensuring that none are active over the pertinent ranges of the coolant flow rate, ϕ , and heat transfer coefficient, χ , between the combustion gas and the solid surface. The analysis has been conducted assuming a ~ 10 -m-span vehicle, three-shock design, with a combustor operating at Mach 7 with hydrocarbon fuel (Table 1). The code provides a basis for selecting preferred materials and identifying directions for the development of advanced materials capable of superior performance at lower weight [5]. Weight is one of the leading factors limiting vehicle performance, especially range [8].

Combustor shapes are compared using performance maps (Fig. 7) and weight charts (Figs. 8 and 9). The maps (Fig. 7) identify the domains in which a material can function without failure, both with and without a (yttria-stabilized zirconia) thermal barrier coating (TBC) [11]. The preferred materials are those that combine the capability for performing at *low flow rates and high heat transfer* and, thereby, enable functionality as close as possible to the upper left corner of the maps. Each map is the result of two independent optimizations. One is performed absent a coating because, when such solutions exist, they are preferred. When solutions only exist with a coating, the optimization is conducted using the TBC thickness as a variable. The charts (Figs. 8 and 9) reveal complementary information, shown here *for the cylindrical model only*. They indicate the minimum mass of combustor panels able to satisfy the performance requirements for fixed χ , but variable ϕ . The results are presented at two different levels of heat transfer ($\chi = 1, 2$).

The code has been used to generate performance maps for a representative group of candidate materials (Table 2; Fig. 7). Each map is the result of two independent optimizations. One (yellow) is performed absent a coating because, when such solutions exist, they are preferred. When solutions exist only with a coating (light gray), the optimization is conducted using the TBC thickness as a variable. Areas without a feasible solution are in white. The maps are ordered

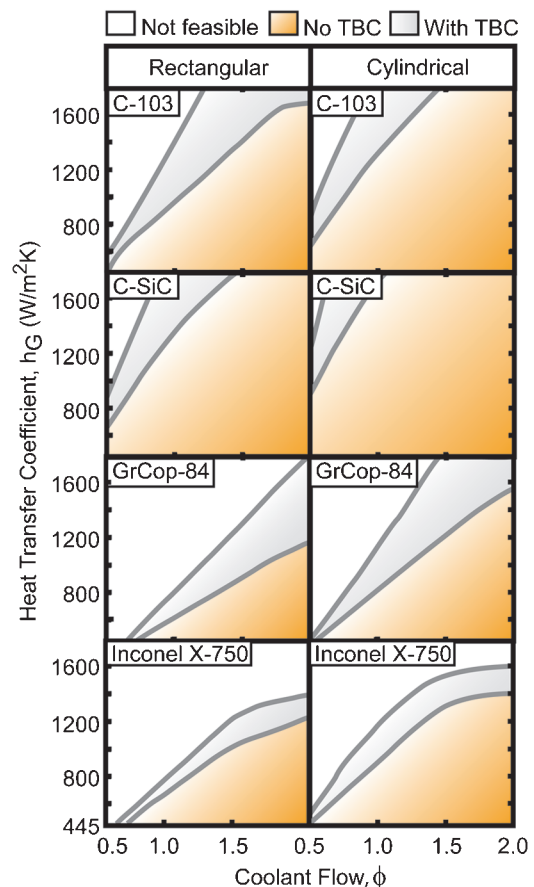


Fig. 7 Performance maps for a number of candidate materials (Table 2) at equal combustor area.

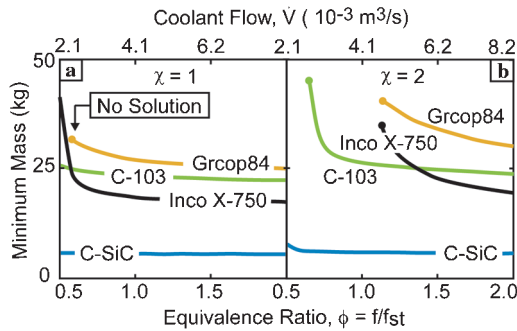


Fig. 8 Weight-performance charts for cylindrical combustors that display minimum panel mass as a function of coolant flow rate for a number of material candidates (Table 2). Results at representative levels of combustion heat transfer ($\chi = 1$ and $\chi = 2$) are presented.

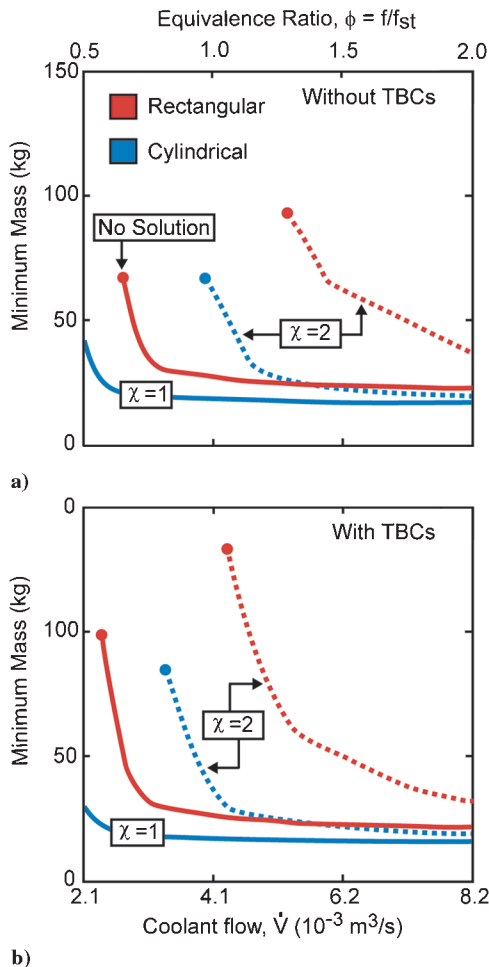


Fig. 9 Specific results obtained using the properties of INCONEL X-750. A comparison of optimal panel weight between cylindrical and rectangular configurations for two levels of heat transfer ($\chi = 1$ and $\chi = 2$): a) without TBCs, and b) with TBCs.

from the most to the least viable. At constant combustor area, the following can be observed:

1) The Nb and C-SiC materials have the largest admissibility domains for both combustor shapes. However, both materials require *environmental* barrier coatings, which are not considered in this analysis [12–15].

2) The performance of each material is enhanced under the cylindrical design. Such designs allow operation with both lower coolant flow rates and higher thermal loads.

The corresponding weight charts (Fig. 8) for the cylindrical model provide a ranking. C-SiC always has the lowest weight. Among the

metallics, the Ni or Nb alloys are the preferred candidates, albeit at more than three times the weight of C-SiC.

A shape comparison of optimal panel weights is presented in Fig. 9 for one of the leading metallic candidates, INCONEL X-750. For both shapes, when required to sustain larger χ , the panel is heavier and the feasibility range in coolant flow, ϕ , is diminished. The cylindrical design provides the lowest weight solution for the two levels of heat transfer investigated. In addition, the cylindrical model also allows operation with lower coolant flow, thereby increasing fuel economy. Recall also, the extra mass of the supporting structure required by the rectangular design is not accounted for in this analysis. The addition of a TBC (Fig. 9b) is shown to be beneficial, especially at lower flow rates and higher heat transfer. *In summary, cylindrical designs provide lighter optimal structures and greater fuel economy.*

VI. Unit-Cell Weight Efficiency in Small-Scale Vehicles

It is unclear how much of the foregoing weight benefit is simply due to the smaller cylindrical perimeter. Moreover, annular vehicles are better approximated as smaller one-shock systems, and as demonstrated in Fig. 6, smaller vehicles exacerbate shape effects. Thus, the model is extended to compare combustor shapes and sizes for one-shock systems based on unit-cell weight efficiency instead of total panel weight. Although results are presented for cylindrical designs, the very same methodology is directly applicable to annular designs (i.e., designs in which combustion occurs in an annular region delimited by two actively cooled concentric cylindrical walls), with the proviso that the total wetted perimeter of the combustor be accounted for in computing the local coolant flow rate in each duct. For Mach 7 flight at 30 km, the thermal and mechanical loads become more benign with decreasing combustor size (Table 1), while the stoichiometric ($\phi = 1$) cooling capacity diminishes [Eq. (7)]. For the following analysis, the more benign one-shock loading conditions are kept constant for each of the three vehicle sizes considered: $R/H_{\min} = 3, 9, \text{ and } 27$. Note that the case $R/H_{\min} = 27$ has the same size combustor as that considered for the foregoing three-shock system. This time, for comparison, three rectangular combustors with areas equal to those for the cylindrical designs are analyzed at the same width/height ($B/H_3 = 3.38$). At constant area, the effect of perimeter on the optimal mass for shape comparisons is eliminated through normalization.

The normalization scheme uses the range of dimensions available to the optimization protocol [5] to find the minimum allowable structural mass for each shape. Given the range of dimensions available to the optimizer, the minimum gages and channel height in combination with the maximum channel width determine the minimum allowable structural mass [5]. In this way, the optimal mass ratio, $\Lambda > 0$, represents the *additional mass needed to survive the thermomechanical loading* (Fig. 10). The optimal mass has been ascertained for the Nb-based alloy C-103 as a function of volumetric flow rate and combustor size. Combustor size is indicated by the cylindrical radius normalized by the minimum allowable panel height. At smaller sizes, material feasibility is diminished due to decreased volumetric coolant flow and coolant velocity. Note that the dimensional values for coolant flow, \dot{V} , are not the same, even though the nondimensional, equivalence range (ϕ) is shared by all. The combined thermal and mechanical effects of panel shape/size on the ability of the design to resist all of the failure modes reveals that the cylindrical model, in addition to yielding the lighter panel, is also more weight efficient on a unit-cell basis. Both shapes become relatively lighter as the size increases and the range of feasible coolant flow rates is enhanced, reflecting the dominant thermal aspect of the optimization (Fig. 5). For a given thermal load, χ , the difference in extra mass between combustor shapes diminishes with combustor size, as forecast by Fig. 6. The cylindrical model's superior weight efficiency is further emphasized by considering that the weight of the structural stiffeners required by the rectangular shape is not included.

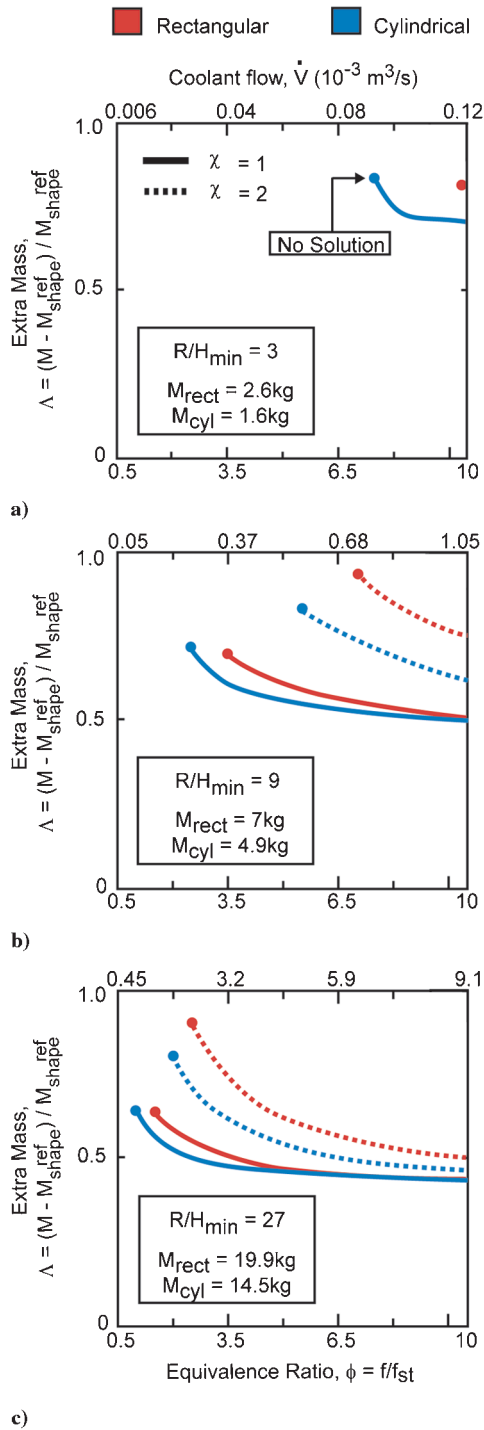


Fig. 10 The cylindrical unit-cell weight efficiency exceeds the rectangular model for a range of combustor sizes. All results are based on a one-shock system (Table 1). Weight efficiency is found as the optimal panel mass relative to the minimum allowable mass for the combustor shape and size considered. Thus, $\Lambda > 0$ is the additional mass needed to satisfy the optimization constraints, plotted as a function of coolant flow rate for the Nb-based alloy C-103.

VII. Conclusions

The characteristics governing the performance of candidate materials used as combustor liners have been analyzed. An understanding of the key design features affecting the thermo-mechanical stress has been established for both cylindrical and rectangular configurations and the range of geometric applicability of the cylindrical model determined. Shape comparisons have been based on equivalent flowpath areas for Mach 7 hydrocarbon-fueled flight. For both shapes, larger combustors require less additional

structural mass to withstand a thermomechanical loading. It emerges from a materials selection perspective that the cylindrical design is preferred because it enhances the feasibility domain (material robustness), while simultaneously providing lighter optimal structures and greater fuel economy.

Acknowledgments

This work was supported by the Office of Naval Research through a Multidisciplinary University Research Initiative program on Revolutionary Materials for Hypersonic Flight (contract no. N00014-05-1-0439). The authors are thankful to David Marshall of Teledyne; Thomas A. Jackson, Daniel J. Risha, and William M. Roquemore of the U.S. Air Force Research Laboratory; and David VanWie of Johns Hopkins University for insightful discussions.

References

- [1] Curran, E. T., and Murthy, S. N. B., *Scramjet Propulsion*, AIAA, Reston, VA, 2000.
- [2] Curran, E. T., "Scramjet Engines: The First Forty Years," *Journal of Propulsion and Power*, Vol. 17, No. 6, 2001, pp. 1138–1148. doi:10.2514/2.5875
- [3] Billig, F. S., and Jacobsen, L. S., "Comparison of Planar and Axisymmetric Flowpaths for Hydrogen Fueled Space Access Vehicles," AIAA Paper 2003-4407, 2003.
- [4] Valdevit, L., Vermaak, N., Zok, F. W., and Evans, A. G., "A Materials Selection Protocol For Lightweight Actively Cooled Panels," *Journal of Applied Mechanics*, Vol. 75, No. 6, 2008, pp. 061022–61037. doi:10.1115/1.2966270
- [5] Vermaak, N., Valdevit, L., and Evans, A. G., "Materials Property Profiles for Actively Cooled Panels: An Illustration for Scramjet Applications," *Metallurgical and Materials Transactions A: Physical Metallurgy and Materials Science*, Vol. 40, No. 4, 2009, pp. 877–890. doi:10.1007/s11661-008-9768-y
- [6] Heiser, W. H., and Pratt, D. T., *Hypersonic Airbreathing Propulsion*, AIAA Education Series, AIAA, Washington, DC, 1994.
- [7] Beer, F. P., and Johnston, E. R., *Mechanics of Materials*, McGraw-Hill, New York, 1981, p. 219.
- [8] Doolan, C. J., "Hypersonic Missile Performance and Sensitivity Analysis," *Journal of Spacecraft and Rockets*, Vol. 44, No. 1, 2007, pp. 81–87. doi:10.2514/1.23160
- [9] Gaiddon, A., Knight, D. D., and Poloni, C., "Multicriteria Design Optimization of a Supersonic Inlet Based upon Global Missile Performance," *Journal of Propulsion and Power*, Vol. 20, No. 3, 2004, pp. 542–558. doi:10.2514/1.2390
- [10] Tan, H., Sun, S., and Yin, Z., "Oscillatory Flows of Rectangular Hypersonic Inlet Unstart Caused by Downstream Mass-Flow Choking," *Journal of Propulsion and Power*, Vol. 25, No. 1, 2009, pp. 138–147. doi:10.2514/1.37914
- [11] Evans, A. G., Clarke, D. R., and Levi, C. G., "The Influence of Oxides on the Performance of Advanced Gas Turbines," *Journal of the European Ceramic Society*, Vol. 28, 2008, pp. 1405–1919. doi:10.1016/j.jeurceramsoc.2007.12.023
- [12] Bewlay, B. P., Jackson, M. R., Zhao, J. C., and Subramanian, P. R., "A Review of Very-High-Temperature Nb–Silicide-Based Composites," *Metallurgical and Materials Transactions A: Physical Metallurgy and Materials Science*, Vol. 34A, 2003, pp. 2043–2052. doi:10.1007/s11661-003-0269-8
- [13] Novak, M. D., and Levi, C. G., "Oxidation and Volatilization of Silicide Coatings for Refractory Niobium Alloys," American Society of Mechanical Engineers Paper 2007-42908, Nov. 2007.
- [14] Webster, J. D., Westwood, M. E., Hayes, F. H., Day, R. J., Taylor, R., Duran, A., Aparicio, M., Rebstock, K., and Vogel, W. D., "Oxidation Protection Coatings for C/SiC Based on Yttrium Silicate," *Journal of the European Ceramic Society*, Vol. 18, 1998, pp. 2345–2350. doi:10.1016/S0955-2219(98)00241-6
- [15] Aparicio, M., and Duran, A., "Yttrium Silicate Coatings for Oxidation Protection of Carbon-Silicon Carbide Composites," *Journal of the American Ceramic Society*, Vol. 83, No. 6, 2000, pp. 1351–1355.